

David J. Quam

Department of Biomedical Engineering,
Marquette University,
Milwaukee, WI 53233
e-mail: dj.quam@gmail.com

Timothy J. Gundert

Department of Biomedical Engineering,
Marquette University,
Milwaukee, WI 53233
e-mail: timothy.gundert@gmail.com

Laura Ellwein¹

Department of Biomedical Engineering,
Marquette University,
Milwaukee, WI 53233
e-mail: laura.ellwein@gmail.com

Christopher E. Larkee

MARquette Visualization Lab (MARVL),
College of Engineering,
Marquette University,
Milwaukee, WI 53233
e-mail: christopher.larkee@marquette.edu

Paul Hayden

Discovery World at Pier Wisconsin,
Milwaukee, WI 53202
e-mail: haydenp@discoveryworld.org

Raymond Q. Migrino

Phoenix VA Health Care System,
Phoenix, AZ 85012;
Division of Cardiovascular Medicine,
Medical College of Wisconsin,
Milwaukee, WI 53226
e-mail: Raymond.migrino@va.gov

Hiromasa Otake

Kobe University Graduate School of Medicine,
Kobe, Japan
e-mail: hiro_yuki15@yahoo.co.jp

John F. LaDisa, Jr.²

Department of Biomedical Engineering,
Marquette University,
Milwaukee, WI 53233;
Director,
MARquette Visualization Lab (MARVL),
Marquette University,
Milwaukee, WI 53233;
Director,
Laboratory for Translational,
Experimental and Computational Cardiovascular Research,
Marquette University;
Medical College of Wisconsin,
Milwaukee, WI 53233;
Division of Cardiovascular Medicine,
Medical College of Wisconsin,
Milwaukee, WI 53233

Immersive Visualization for Enhanced Computational Fluid Dynamics Analysis

Modern biomedical computer simulations produce spatiotemporal results that are often viewed at a single point in time on standard 2D displays. An immersive visualization environment (IVE) with 3D stereoscopic capability can mitigate some shortcomings of 2D displays via improved depth cues and active movement to further appreciate the spatial localization of imaging data with temporal computational fluid dynamics (CFD) results. We present a semi-automatic workflow for the import, processing, rendering, and stereoscopic visualization of high resolution, patient-specific imaging data, and CFD results in an IVE. Versatility of the workflow is highlighted with current clinical sequelae known to be influenced by adverse hemodynamics to illustrate potential clinical utility. [DOI: 10.1115/1.4029017]

1 Introduction

CFD is often used to study hemodynamic indices (those associated with the movement of blood) within computer-based vascular models generated from medical imaging data. This process generally involves creating a vascular model, discretizing it into a finite-element mesh containing millions of pieces (typically tetrahedrons or hexahedrons), specifying rheological properties such

as density and viscosity, prescribing the hemodynamic state at the entrance and exit of vessels (i.e., boundary conditions), and solving applicable governing equations using high-performance computing. Subsequent results, such as wall shear stress (WSS, the tangential force experienced by a vessel due to flowing blood), have been linked to the onset and progression of cardiovascular disease and can therefore be used to augment information obtained in a clinical setting [1–4]. CFD produces time-varying simulation results for the model's millions of elements during an entire cardiac cycle, but the traditional way of displaying these results involves viewing multidimensional indices in two dimensions at a single time point, or average of multiple time points, and a predetermined spatial configuration. This can be done through basic projection onto a 2D plane or through more sophisticated methods to prepare the data for display with traditional screens [5]. In so doing, relationships between vessel features,

¹Present address: Department of Mathematics and Applied Mathematics, Virginia Commonwealth University, Richmond, VA 23284.

²Corresponding author.

Manuscript received November 22, 2013; final manuscript received August 5, 2014; published online January 29, 2015. Assoc. Editor: Ender A. Finol.

This material is declared a work of the U.S. Government and is not subject to copyright protection in the United States. Approved for public release; distribution is unlimited.

such as geometry, hemodynamic indices, and atherosclerotic plaque morphology or neointimal growth, can be masked or not fully analyzed by clinical stakeholders.

IVEs provide large scale, high resolution displays that physically surround users with computer-generated images to create the impression of a virtual world. Advanced visualization techniques, such as IVEs, coupled with stereoscopic rendering capabilities can mitigate some of the traditional 2D limitations mentioned above by improving depth cues and facilitating motion. IVEs are routinely used for other disciplines within academic and industry settings, including medical applications [6–9]. For example, virtual 3D simulation has been successfully used to create radiotherapy plans in prostate cancer patients that result in dosimetric advantage through use of noncoplanar beams [10]. Chu et al. also showed in a randomized study that 3D holographic display led to improved radiotherapy plans in a majority of cases compared to those developed with 2D displays [11]. Immersive 3D platforms also have tremendous potential for training and education in oncology [12] and laparoscopic skills in novice trainees as compared to traditional 2D imaging [13].

The advancements afforded by IVEs also facilitate simultaneous viewing of multiple modalities that is particularly exciting for improved disease characterization and longitudinal study when used with CFD. IVEs were first used with CFD over a decade ago to explore datasets using idealized representations of grafted coronary arteries [14]. Marked advances in high performance computing, computer graphics, and patient-specific CFD modeling have occurred since this time that allow for the study of more complex models. For example, a recent investigation demonstrated that the entire patient-specific CFD modeling process including model construction, simulation and quantification of results in the carotid arteries is feasible within 49 h, most of which were dedicated to simulation and quantification [15]. With this timeline, it is conceivable for CFD to be used within a clinical setting to augment plaque or disease morphology and flow information obtained from routine imaging modalities. A workflow to capture and present spatiotemporal data and simulation results on this timeline is an important step toward creating a tool that can be used by clinicians and engineers to better appreciate the full extent of patient-specific CFD results together with their associated imaging data within an IVE. Based on the established medical applications using IVEs mentioned above, the potential additive clinical utility of IVEs for image-based CFD is expected to be enhancement of disease and pathophysiologic understanding, as well as enhancement of interventional procedure planning including more nuanced plaque-specific decision-making such as selection of stent type, size and orientation, or improved understanding of potential clinical risks of intervention with improved spatial understanding of regional distribution of vulnerable plaques. In addition, 3D stereoscopic visualization may assist engineers and clinicians in avoiding misinterpretations of the visualized information by presenting the information in a natural 3D visual environment rather than the current method of interpreting 2D tomographic slice information and imagining component connections by switching back and forth between various image slices.

The objective of the current work is therefore to highlight the development of a semi-automatic workflow for the import, processing, rendering, and stereoscopic visualization of high resolution, patient-specific CFD results in an IVE. In doing so, we sought to simultaneously view spatiotemporal simulation quantities such as indices of WSS and velocity with their relationship to vessel pathologies within the IVE. The investigation begins with a brief review of current patient-specific simulation capabilities followed by presentation of the semi-automatic workflow for preparing CFD results for viewing in a full-scale IVE. We demonstrate the workflow with two case studies using patient-specific CFD models generated from the left common carotid artery (LCCA, case 1) and left-circumflex coronary artery (LCX, case 2). Though the purpose of the current work is to highlight the development and versatility of the workflow, each example focuses on current

clinical sequelae and potential sources of long-term morbidity thought to be influenced by adverse hemodynamic alterations and highlights the potential clinical utility to be expanded upon in future work leveraging the methods presented here.

2 Methods

The immersive visualization method described here is divided into four stages (Fig. 1) that rely on the use of software facilitating immersive, stereoscopic rendering (i.e., IVE Software). These stages include: (1) obtain vessel morphology and model creation, (2) applying boundary conditions and simulation, (3) postprocessing, and (4) presentation. Stages 1 and 2 are common to many vascular CFD studies, while stages 3 and 4 are the focus of the current work and present new methods applied beyond conventional CFD processing. These stages are discussed in detail below after briefly introducing the software used to implement them.

2.1 IVE Software. We employed EON STUDIO 7 [16] for the workflow because of its compatibility with available hardware and use within a local IVE facility where a version of the current results is displayed for informal science education as discussed in more detail below (please see Sec. 2.6). The software architecture of EON STUDIO uses a task-specific, hierarchical, modular structure. The hierarchy decreases rendering time and allows for a greater level of control in specifying what combinations of modules are realized. When specific combinations of these modules are applied to input data, the desired output can be obtained and rendered. The file system employed by EON aggregates the necessary data for the simulation into a single resource file, making storage and transport of the IVE content simple since only two files must be managed by the user. The EON package has a software layer to allow source code to be supplied to automate the assembly and programming of these modules. EON also includes a module to support multiwall immersive rendering. EON uses the Microsoft DirectX graphics library, which facilitates rendering on a variety of display formats.

2.2 Obtaining Vessel Morphology and Model Creation. The construction of patient-specific CFD models of the flow domain begins with the acquisition of 3D medical imaging data composed from a series of 2D planar images (Fig. 1(a)). The deidentified images here were obtained from research subjects who provided informed consent to participate in imaging research studies under the supervision of the Institutional Review Board and Ethics Committee at the Medical College of Wisconsin and Kobe University, respectively. The 2D planar images are segmented by clinicians to identify the important landmarks including the lumen and vessel wall. For case 1, LCCA segments and plaque components were delineated by clinicians using Magnetic resonance (MR)-Plaqueview (VP Diagnostics, Seattle, WA) as previously described [15]. For case 2, lumen and stent segments were obtained and delineated by clinicians using a commercially available optical coherence tomography (OCT) imaging system with associated software [17] (LightLab, St. Jude Medical, Westford, MA). In each case, the segmented imaging data are then lofted to create patient-specific 3D vascular models (Fig. 1(b)) [15,18–20]. In some models (e.g., case 2), a stent is virtually implanted (Fig. 1(c)) using a rapid virtual implantation process consisting of a series of Boolean operations to remove portions of the flow domain that are not available for blood flow due to the presence of stent linkages [21]. An adaptive meshing algorithm [22,23] was then applied when discretizing the model into its finite-element mesh (Fig. 1(d)) of tetrahedral elements using MeshSim (Simmetrix, Clifton Park, NY). Isotropic meshes were first run for each case before successive adapted meshes were created as described elsewhere for stented [21,24,25] and unstented arteries [15,26].

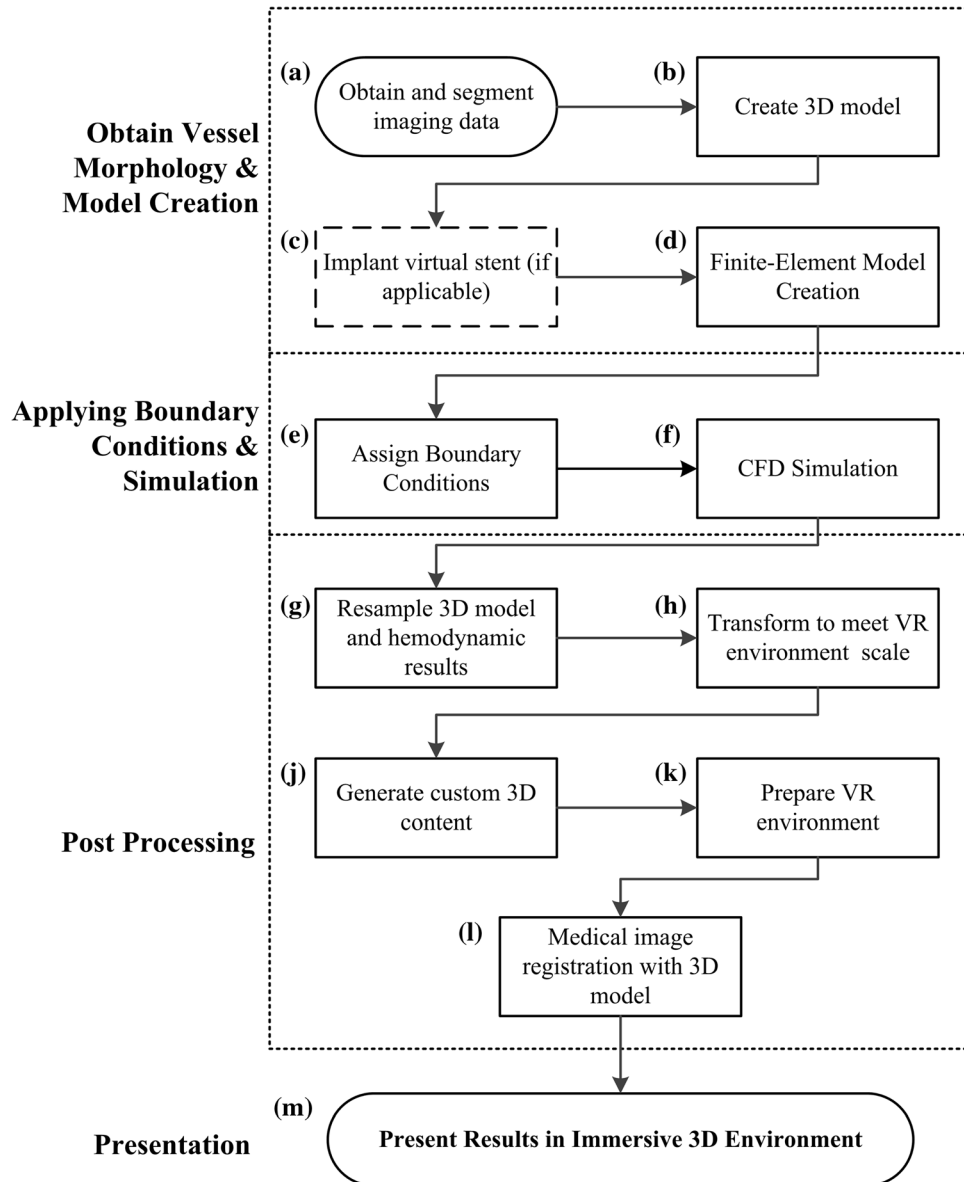


Fig. 1 Flowchart describing the immersive visualization workflow. Steps a–f are common to many vascular CFD studies, while steps g through m are the focus of the current work and present new methods applied beyond conventional CFD processing. Medical imaging data is obtained and segmented (a) to create a 3D model (b) of the vasculature. In some cases, a stent is virtually implanted (c) prior to creating the finite-element model (d). Boundary conditions are then applied (e) before conducting a CFD simulation (f). The postprocessing stage begins by resampling the 3D model and hemodynamic results (g), the data is then transformed to meet the scale of the IVE (h) and custom 3D content is generated from the simulation results (i). The data is then prepared for the IVE (j) and the medical images are registered with the 3D model (k) prior to presentation in the IVE (m).

2.3 Applying Boundary Conditions and Simulation. Boundary conditions are applied to the model prior to CFD simulation (Fig. 1(e)). Inflow boundary conditions consisting of time-varying blood flow waveforms were imposed at the inlet of each model based on either a normalized waveform that was scaled to the patient's body surface area (case 1) [15,27] or a canine waveform with values for Reynolds and Womersley numbers similar to those found in humans (case 2) [18,28]. Outlet flow boundary conditions are prescribed using a three-element Windkessel model based on measured or estimated blood pressure using the pulse pressure [29,30] and coupled-multidomain [31] methods described in detail previously. The Windkessel model serves as a surrogate for the downstream impedance to blood flow

and arterial capacitance [25,31,32]. Values used for each case are provided in Table 1. Additionally, a no-slip boundary condition is imposed at the vessel wall and blood was assumed to behave as a Newtonian fluid (4 cP) with a constant density (1.06 g/cm³). CFD simulations were performed using an in-house stabilized finite element solver with a commercial linear solver component: LESLIB (Altair Engineering, Troy, MI) to solve the time-dependent Navier–Stokes equations (Fig. 1(f)) [33]. The time-step was chosen for a Courant, Friedrichs, and Lewy condition <1. Standard convergence criteria were employed and simulations were run until the outlet pressure and flow were periodic, defined as a maximum error between equivalent points in successive cardiac cycles <1 mmHg and <1 mm³/s.

Table 1 Outlet boundary conditions for case studies using patient-specific CFD models generated from the LCCA and LCX

Case	Artery	Branch	characteristic resistance (dyn·s·cm ⁻⁵)	Capacitance (cm ⁵ /dyn)	distal resistance (dyn·s·cm ⁻⁵)
1	LCCA	Internal	3260	5.25×10^{-5}	23,100
		External	7600	2.25×10^{-5}	53,900
2	LCX	Distal LCX	44,800	6.1×10^{-7}	188,000
		2nd obtuse marginal	30,300	4.7×10^{-7}	273,000

2.4 Postprocessing. Postprocessing techniques were deliberately implemented to convert the output format of medical imaging data and results from the CFD solver into the volumetric and quantitative requirements of the IVE display software using the steps below.

CFD results are processed using MATLAB (The MathWorks, Natick, MA). MATLAB was selected for three reasons. First, our institution maintains an active license, and it therefore represents a tool that is likely to be available to future users of these methods. Familiarity with MATLAB is also extensive and allows for the scripts to be understood by many users. Second, our research group has a large repository of existing postprocessing methods written in MATLAB for conducting separate CFD postprocessing. Using MATLAB for the postprocessing methods described here extends these methods without introducing a new programming language and allows some of the current methods to build from existing ones. Third, MATLAB allows easy construction of graphical user interfaces (GUIs) using a built-in tool called GUIDE.

All postprocessing steps using MATLAB discussed below have been combined into a single executable file with the GUI. The GUI clearly specifies the files necessary to carry out the postprocessing steps. It also provides an easy to use interface through which the user can locate files that may be in various locations. The GUI also enforces the types of files input to the algorithms. For simulations that conform to the expected use case, pressing a “Generate Files” button will correctly apply each of the postprocessing steps described in this section. Individual steps can also be isolated from the rest of the process and executed separately. A detailed description of the GUI’s operation can be found elsewhere [34].

The GUI mentioned above calls separate MATLAB scripts for blood flow velocity, blood pressure, instantaneous WSS, time-averaged WSS (TAWSS), oscillatory shear index (OSI, a measure of the directionality of WSS ranging from 0 to 0.5, where 0 indicates that WSS is unidirectional, and 0.5 indicates bidirectional WSS with a time-averaged value of zero) as discussed in more detail for each simulation result below.

Blood flow velocity is visualized with vectors (arrows) indicating flow direction during the cardiac cycle. This information is directly extracted from the CFD results. However, CFD results often contain velocity information for millions of spatial coordinates, and it is computationally expensive to render and visualize this large amount of data. Therefore, a MATLAB script is used to extract the spatial locations for a smaller subset of velocity vectors (~0.1%) that are uniformly distributed. The distribution is controlled by the user with two spacing parameters: the proximity to other vectors and the minimum distance from the vessel wall. A portion of vectors are placed in close proximity to the vessel wall to appreciate the no slip condition imposed. For each vector location, the orientation is calculated at each time point in the cardiac cycle and indicated by the direction of the vector’s arrow, while the vector’s length and color denote the magnitude of its velocity. The color is determined through a lookup table, whereby the scalar value of the velocity magnitude is compared to a red/green/blue (RGB) color code. The results for blood flow velocity are calculated using the following steps:

Place vector origins in vessel volume per spacing parameters

Write vector node locations to File A

For each time point t:

For each vector origin n in File A:

Apply transformation matrix

Convert velocity vector to Euler angles

Calculate associated color value

Write Euler and color values to location n in File B_t

End

End

WSS, TAWSS, and OSI are all visualized on the vessel wall. The vessel wall is extracted from the CFD mesh and saved as a separate 3D unstructured grid (i.e., a list of nodes and their connectivity). A unit normal vector is computed at each node and saved as part of the unstructured grid. This facilitates the use of continuous shading algorithms, such as Gouraud or Phong, for the surface within the IVE. The magnitude of the time-varying WSS at each node is extracted directly from the CFD mesh, but TAWSS and OSI require additional computations. TAWSS is computed at each node on the surface of the CFD mesh as shown below

$$\text{TAWSS} = \left| \frac{1}{N} \sum_0^N \overrightarrow{\text{WSS}} \right| \quad (1)$$

where WSS is stylized as a vector and N is the number of discrete time points in one cardiac cycle. OSI is computed at each surface node as shown below:

$$\text{OSI} = \frac{1}{2} \left(1 - \frac{\left| \frac{1}{N} \sum_0^N \overrightarrow{\text{WSS}} \right|}{\frac{1}{N} \sum_0^N |\overrightarrow{\text{WSS}}|} \right) \quad (2)$$

Similar to the velocity vectors, the magnitude of WSS, TAWSS, and OSI are depicted on the vessel surface with using an RGB color map. The following steps were applied for each hemodynamic index with the exception of velocity:

For each time point t:

For each node n in File A:

Apply transformation matrix

Calculate scalar value and associated color value

Write values to location n_t in File B

Determine connectivity to other nodes

Write connections to location n_t in File C

Calculate surface normal

Write vector to location n_t in File D

End

End

In addition to the 3D hemodynamic and structural data that is displayed in the IVE, a blood pressure waveform can be toggled to display on a static 2D heads-up display (HUD) within the IVE. The blood pressure at the inlet of the CFD model is extracted

from the simulation results during one cardiac cycle to produce a plot of pressure versus time. The IVE software maintains an internal chronometer that synchronizes events in time. When this plot is displayed in the IVE, an indicator such as a vertical dash or circle therefore moves to indicate the time in the cardiac cycle to which time-varying quantities, including velocity and WSS, correspond. The HUD is also used to display the RGB color maps of the various hemodynamic data displayed in the IVE, and can be used to also toggle on a display of the user's relative location in the vessel or name of the vessel within the current anatomical location.

The final step in the postprocessing stage is to register the medical imaging data with the CFD model (Fig. 1(l)). It is common for more images to be acquired than can be reasonably displayed in the IVE. For this reason, a subset of the evenly dispersed imaging data is displayed in the IVE. 3D image planes are created in virtual space for each image selected for registration with the CFD model. A transformation algorithm applies rotations specified by the imaging modality. These rotations may be identical for all image planes (e.g., MR imaging, computed tomography) or a unique rotation calculated for each image (e.g., OCT, intravascular ultrasound) depending on the imaging modality. The IVE software describes rotations in terms of roll (counterclockwise about the x -axis), pitch (y -axis), and yaw (z -axis). By applying specific transformations to images used to create the vessel geometry (please see Sec. 3.1), we ensure that each experience in the IVE represents the CFD results in a consistent manner. Modality-specific details of this step are presented in Sec. 2.5. The resulting planes intersect the vessel model at locations and orientations that reflect the relative positions of the anatomy and images at the time they were acquired. In general, the following steps are required to transform the images to be aligned to a 3D model:

```
For each image p:
    Calculate 3D angular deviation from vessel
    centerline
    Convert angle to Euler coordinates
    Write data to File A describing image
    orientation
End
Load File A into simulation software
```

2.5 Presentation. Postprocessed CFD results are imported into the IVE software using custom Visual Basic (VB) scripts that control where the data are stored within a hierarchical, modular structure (Fig. 1(k)). This hierarchy decreases the time required to access the data and allows a greater level of control in specifying custom visualization features such as opacity and brightness. The VB script steps followed by the IVE software are described below:

```
Link to directory containing geometry
Create temporary vector data storage
Create shape object
For each node in Nodes file:
    Load vector data
    Load normal data
Load connectivity data from Connectivity file
Apply appearance settings
```

The vessel geometry data file is read by a VB script and converted to a 3D mesh representing the vessel lumen. If present, the stent geometry file is also converted to a solid structure and embedded into the vessel model. The VB scripts then automate the process of creating a unique simulation element for each data point in the source file, where the end result is a full model of the vessel. Time-varying simulation results are treated as separate files for each time point in the cardiac cycle when imported to the

IVE. When requested by the user, each file is read, processed, and rendered in real-time to produce the effect of motion in the IVE.

Since the medical images are produced in accordance with the DICOM standard and the results produced by the CFD solver used in our lab are written in a common format (Visualization Toolkit³), the methods described can likely be applied to many other IVE display software packages capable of using these formats with only modest modifications.

2.6 IVE System. We present results in an IVE called the human interactive virtual education (HIVE) system, located within Discovery World at Pier Wisconsin, a facility specializing in informal science education and programming (Milwaukee, WI). Figure 2 shows a male of average height standing within the HIVE as well as a schematic diagram and illustration of the system components. Stereoscopic 3D rendering is accomplished using CrystalEyes 3 active shutter glasses. The HIVE is an IVE equipped with four Christie Digital Mirage S + 2K HD projectors having a display frequency of 100 Hz and 4 HP Z800 Workstations (additional specs: Intel Xeon E5630 2.53 GHz processor, 12 GB RAM, Windows 7 64-bit, and Nvidia Quadro 6000 with G-Sync cards). The HIVE is designed in the style of the cave automatic virtual environment (CAVE) in which the user is surrounded by content on several screens [35] thus providing the requisite sense of immersion and improvements in depth cues afforded by IVEs. The HIVE system employs four screens (front, left, right, and floor; Fig. 2) providing large $10' \times 8'$ images with a resolution of 1400×1050 pixels per screen. When considering the example cases presented here, this provides a magnification of approximately 300- and 800-fold relative to the approximate vessel diameters for the LCCA and LCX, respectively. Vessel models are scaled by a constant factor to maximize the field of view (FOV) when rendered in the IVE. The factor varies based on the original size and orientation of the vessel in space. In addition to scaling, the vessel is translated to fix its geometric center at the origin of 3D space. The hardware associated with this IVE supports head-tracking functions using a 7 camera Vicon IR tracking system, but we elected not to use this feature as the cases presented intend for the system be used as a collaborative tool by multiple clinicians. If the navigation of the visualization content were linked to a single user's point of view, the tracked user's motion would create artifacts for the other users that likely reduce their comfort. The immersive analysis of CFD results is conducted in active 3D stereoscopy (Fig. 1(m)). The IVE software visualization file must be configured for projection in the IVE by establishing the size and relative location of each screen. The hardware and software coordinate the timing of the active image to the correct eye by emitting an infrared burst, which signals the active shutter glasses to alternate the active lens to opposite eyes.

3 Results

The presentation of CFD results from the immersive visualization method described above is described here for two regions of the vasculature to highlight the workflow's flexibility in application. The LCCA and LCX were modeled, simulated, and rendered in the HIVE. Due to inherent differences in the structure of the vessel and the imaging modalities used to acquire them, the details of application differ slightly among the imaging modalities and are discussed here.

3.1 Modality-Specific Postprocessing. In preparing the vessel geometries for use in the IVE, they are rotated such that the principal axis of the vessel is parallel to the floor of the IVE. This ensures that the initial viewing angle in the IVE has a sufficiently wide FOV to observe all parts of the vessel. The LCCA is rotated 235 deg about its Z axis, whereas the LCX is rotated 190 deg to

³www.vtk.org

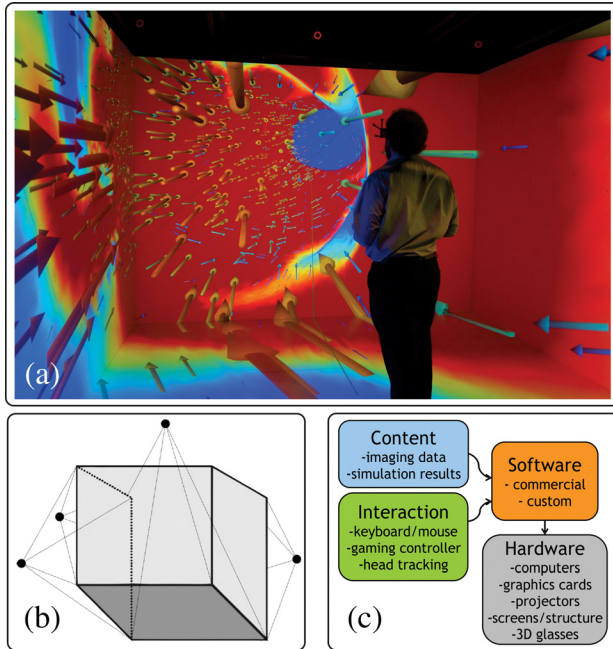


Fig. 2 A male user of average height is shown standing within the four-walled IVE of the current investigation (a). The LCCA CFD results have been rendered within the IVE and the user is wearing active shutter glasses to allow him to view the results of the workflow in stereoscopic 3D. Blood velocity is communicated by the length and color of the velocity vectors that are pointing into the plane of the screen. A pressure versus time curve plotted with a temporal indicator to communicate position within the cardiac cycle can also be toggled on in the upper left corner of the front screen. A spatial indicator of location within the artery can similarly be toggled on. A schematic illustration of the IVE is shown in (b). The black dots in the image represent high-resolution projectors. The front and side screens are rear-projected, while the floor is top-projected. A schematic illustration of the system components is also provided in (c).

achieve the same result. Both arteries are rotated -90° about the Y axis. This difference originates from the original orientation of the CFD models, which are based on the orientations of the vessel within the patient's anatomy. The LCX is also scaled by a factor of 2.85 in all three directions, whereas the scale of the LCCA remains at 1. These results are summarized in Table 2.

Blood flow velocity vectors vary in magnitude relative to their location within the vessel and time during the cardiac cycle. The user is also able to visualize the directionality of the blood at each point in the cardiac cycle using these vectors. The scaled LCCA case spaces vectors with an average intravector distance of 1.5 mm and the minimum distance between a vector and the wall is 0.5 mm. Placing the vectors near the wall illustrates the no-slip condition imposed at the wall and also makes the visualization of areas of flow reversal possible because we are able to see the direction of the velocity arrows reverse, indicating retrograde flow. An intravector spacing constant of 3.0 and minimum wall constant of 1.0 were used for the LCX case. The LCX case presented here requires a greater spacing between velocity vectors due to its associated increased blood flow velocity. These settings applied for the LCCA and LCX (Table 2) not only decrease the density of the vectors in each artery but also decrease the computational expense associated with rendering a large number of elements.

Figure 3 demonstrates the image registration techniques developed and applied to the LCCA from MR images. We have also applied this method to the LCX from OCT imaging as seen in Fig. 3. The LCCA MR images are acquired in the anatomical

Table 2 Summary of transformation parameters for case studies using patient-specific CFD models generated from the LCCA and LCX

Transformation	LCCA	LCX
Z rotation (deg)	235	190
Y rotation	-90	-90
Scale (unitless)	1.0	2.853
Velocity vector spacing (intravector/wall distance; mm)	1.5/0.5	3.0/1.0

transverse plane, such that they are generally aligned orthogonal to the vessel's central axis. For this reason, registration of MR images only requires the images to be spaced evenly to correspond to their slice thickness (i.e., 2 mm in this case) [15] and processed to show plaque components (slices A–E of Fig. 3) with general morphology. In contrast, OCT imaging does not necessarily produce images orthogonal to the vessel's central axis since the images are acquired as an imaging wire is retracted through the artery. We therefore determine the most probable path taken by the imaging wire as discussed in detail elsewhere [18] and then position the OCT images perpendicular to this path. Equations (3) and (4) describe the angles calculated at the lower left corner ordered pair (x, y) of each image coordinate in the virtual space, where z is the depth dimension. Equations (5) and (6) show the rotation matrices used to first rotate the image plane about the Y axis then the X axis. The combination produces the orientations in the LCX portion of Fig. 3

$$\alpha = \arctan\left(\frac{x}{z}\right) \quad (3)$$

$$\beta = \arctan\left(\frac{y}{x\sin(\alpha) + z\cos(\alpha)}\right) \quad (4)$$

$$R_y = \begin{bmatrix} \cos\alpha & 0 & -\sin\alpha \\ 0 & 1 & 0 \\ \sin\alpha & 0 & \cos\alpha \end{bmatrix} \quad (5)$$

$$R_x = \begin{bmatrix} 1 & 0 & 0 \\ 0 & \cos\beta & -\sin\beta \\ 0 & \sin\beta & \cos\beta \end{bmatrix} \quad (6)$$

3.2 Presentation of Results. TAWSS for the LCCA and LCX have been coregistered with imaging data in Fig. 3 (slices C and K, respectively) by the use of the rotation matrices above. Slice C of Fig. 3 highlights a feature of the framework designed to selectively show slices nearest the viewer's vantage point. As the user's virtual location in the vasculature approaches the slice's location, the slice will appear while the others decrease in opacity. This feature allows users to focus only on a single slice, and better appreciate its contents.

Velocity information from the LCCA is shown in Fig. 4, where CFD results from three points in the cardiac cycle have been shown. The velocity inserts shown indicate both the direction and magnitude of blood flow at a particular point in time. This information is useful in understanding complex flow patterns during the course of the cardiac cycle. TAWSS and OSI have also been rendered in Figs. 4(d)–4(f).

Figures 3–5 also demonstrate how the results generated by the workflow yield high resolution viewing to deliver a compelling, immersive experience that limits external stimuli and generates large and vivid representation of the imaging data and simulation results consistent with prior accounts of IVEs [36]. The velocity vectors described previously are seen pointing into the plane of the screen, indicating that blood is flowing in this direction.

Navigation in 3D virtual space requires understanding of the software settings employed as well as relative boundaries within

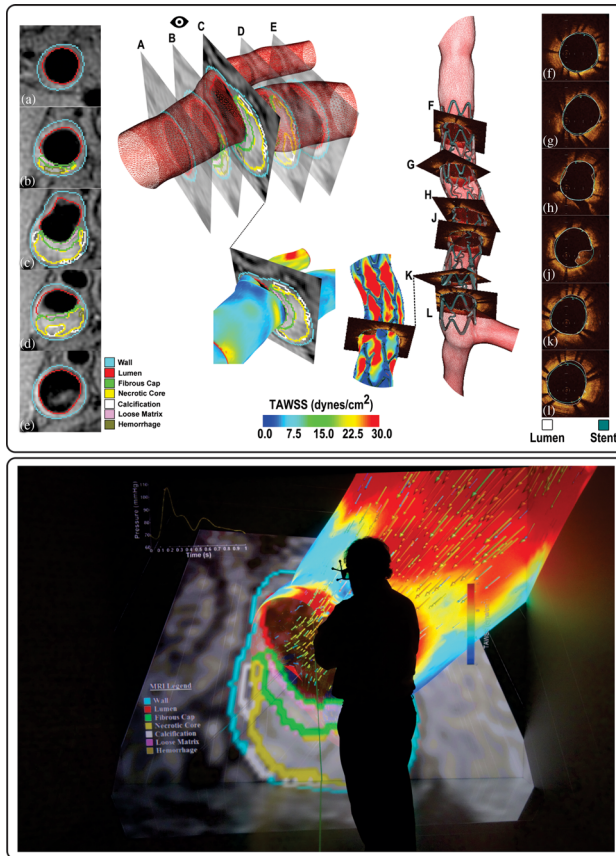


Fig. 3 3D rendering of spatial image orientation for cases 1 and 2. Slices A–E have been segmented to differentiate the plaque morphology according to the legend on the bottom left. In each slice the inner-most layer (the lumen) is used to create the vessel model. The MR acquisition sequence collects axial images. The eye icon indicates the user's position in virtual space, which controls the opacity of slices in close proximity. OCT images (F–L) are acquired in such a way that images are not necessarily orthogonal to the vessel's central axis. The outline of the stent and lumen are well resolved as seen in the turquoise and white traces, respectively. The thrombus seen in slice J is well resolved with OCT. TAWSS is colocalized with the respective medical imaging modalities for both cases. At lower left the user can appreciate the colocalization of the region of low TAWSS with increased wall thickness (slice C). At lower right, OCT images elucidate the relationship between stent location and regions of altered TAWSS (slice K). The image on the bottom of the figure shows a user viewing LCCA imaging data, spatially colocalized TAWSS results, and peak systolic velocity vectors within the IVE used for the current investigation. Note the differences in scale between TAWSS in the LCCA results shown in the top (0–30 dyn/cm²) and bottom (0–15 dyn/cm²) images.

the region of the vasculature being studied. To mediate this, we developed a method of navigating the virtual space that supplies the user with a set of predetermined vantage points programmed to highlight the regions of highest clinical utility. When the user selects a vantage point using the computer terminal the IVE software interpolates a smooth camera transition to the next vantage point following a cubic spline path. In addition to making navigation more intuitive and rapid, the predetermined vantage points also increases user comfort while using the IVE by interpolating between vantage points in a way that does not cause motion sickness. The determination of vantage points was made based on a priori knowledge of the locations of atherosclerotic or neointimal growth within the cases. Figure 5 outlines the vantage points that were predetermined for the LCCA case. Importantly, this

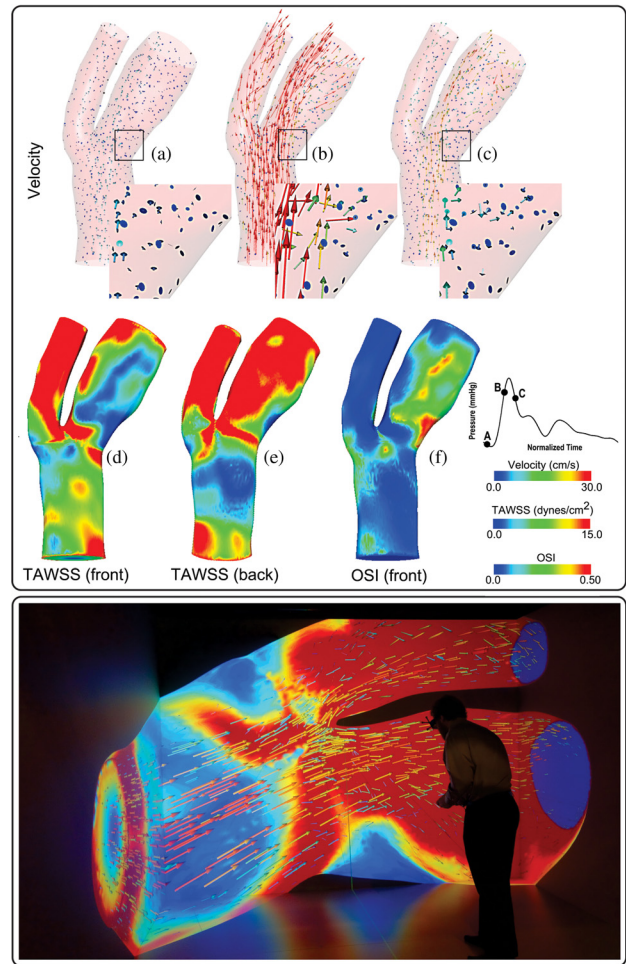


Fig. 4 Temporal and time-averaged hemodynamic quantities rendered in IVE. a–c show velocity vectors at specific temporal locations as indicated on the corresponding pressure waveform. The velocity is communicated by the vector magnitude and color; after reaching maximum velocity immediately prior to peak systole, the velocity decreases with time. The collection of velocity results are used to create TAWSS results as visualized in (d) and (e). The inset of velocity images (c) also shows a region of flow reversal which is consistent with the high values of OSI (f). The image on the bottom of the figure shows a user viewing LCCA velocity vectors within the IVE used for the current investigation. The velocity vectors correspond to the time denoted by time point B (b) above, and the user has navigated into the vessel so that TAWSS on the back (e) of the LCCA is being viewed simultaneously.

process could be automatically implemented into the workflow shown here. The predetermined vantage points are easy to use when navigating through the immersive visualization of data and results by the use of shortcut keys. However, it is possible to use manual navigation via standard up/down, left/right, and forward/back commands or interaction devices such as the Flystick series of products by Advanced realtime tracking (ART, Germany). Such manual navigation allows the users to more closely explore any section of the vessel's anatomy that may prove to be interesting, yet not included in the predetermined vantage points. Further, these points can be set dynamically and are not hard coded into the simulation file itself.

4 Discussion

The objective of the current work is to highlight the development of a semi-automatic workflow for the import, processing,

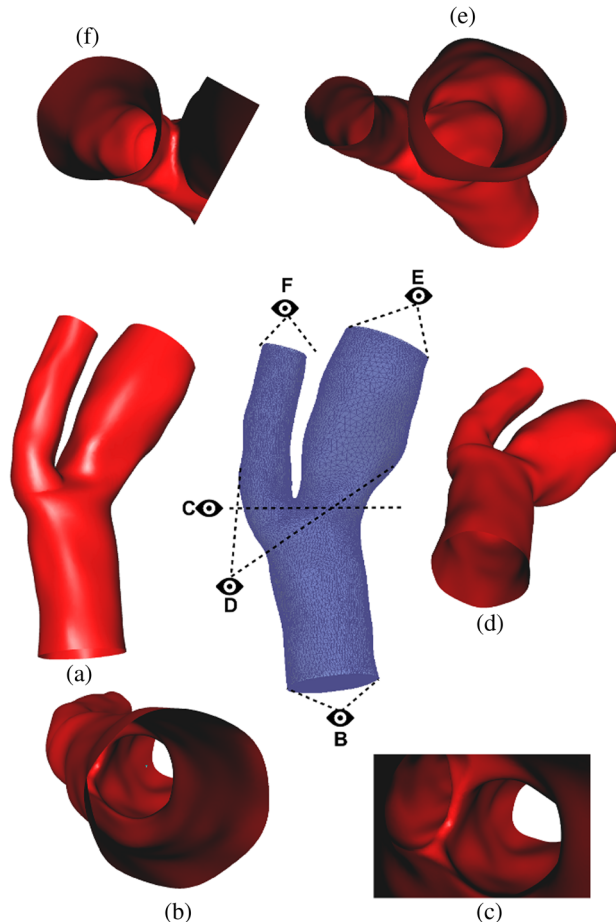


Fig. 5 Predetermined vantage points facilitating smooth navigation during collaboration for the LCCA case. (a) shows the entire section from a wide vantage point. (b) shows the vantage point viewing into the vessel in the direction of blood flow proximal to the carotid bifurcation. (c) shows a vantage within the vessel upstream of the flow divider. (d) is an external view of the LCCA that is optimized for viewing the MR imaging slices. (e) and (f) show the vessel distal to the bifurcation, in each respective daughter branch.

rendering, and visualization of high resolution, patient-specific hemodynamic data and CFD results in an IVE. In many cases, the workflow can be rapidly applied (<60 min), with much of the time dedicated to computation. Previous work done to integrate CFD with immersive visualization has used idealized vascular representations of a single region of the vasculature, rather than patient-specific models shown here [14,37]. Whereas previous work [14] emphasizes developments made in data interaction and user interfaces, the current investigation serves two purposes: first, to highlight the semi-automated workflow and second, to present results supporting further development of these techniques in order to gain additional scientific insights pertaining to clinical sequelae that can be quantitatively explored with the current method. We have highlighted three ways the workflow presented here begins to accomplish this goal: First, the workflow preserves the natural appearance of medical imaging data as the user approaches its spatial location during navigation. This avoids misinterpretation of the visualized information by presenting the information in a more natural manner rather than the current method of interpreting 2D tomographic slice information and imaging component connections by switching back and forth between various image slices. Second, the workflow allows for gradual transition between predetermined vantage points during navigation. For our applications, the vantage points are set by

anatomical landmarks, as well as engineering metrics of interest such as low TAWSS within the LCCA, or pathologic regions of concern including the presence of thrombus within the LCX after stenting. Third, the workflow facilitates both immersion and stereoscopic viewing beyond what is routinely implemented for visualizing CFD results. The IVE places the user in a virtual world of the imaging data and greater detail from CFD results thereby augmenting the level of immersion experienced. The HIVE system used here also offers a wide FOV, allowing the user to see a nearly panoramic view of the hemodynamic data and results. These two factors are important considerations in a system's ability to provide an immersive environment [36]. Standard 2D and 3D desktop monitors are capable of rendering scenes as though observed through a window, in which the user has a limited vantage point and ability to interact with the data [37]. In contrast, IVEs provide the user with a more tangible way of actively learning by interacting with the data in the virtual environment with improved depth cues. It has been shown that when viewed from multiple angles and orientations, individuals better understand and retain spatial information and understand complex phenomena [38,39]. In general, when simulation software alters the rendered image in response to a user's command the sense of interaction is enhanced.

4.1 Case Study 1: Carotid Artery. In the first case study, we present results obtained from an LCCA with MR imaging. Our method places the medical imaging data atop the solid model to display both structural and functional data simultaneously. The increased wall thickness in slices C and D of Fig. 3 can be further appreciated when viewed in an IVE because they are seen relative to the vessel length and diameter. This information can help the user establish a 3D mental image of the LCCA vasculature and appreciate any vessel narrowing or concerning areas. Such knowledge may be useful in clinical settings when planning procedures or analyzing results of medical imaging protocols.

Figure 3 illustrates regions of low TAWSS being localized with developing atherosclerotic lesion as seen by the colocation of the fibrous cap/necrotic core at slice C. The user can appreciate the instantaneous or TAWSS values as they relate to the vessel surface and segmented image slices building off of previous studies demonstrating the localization of atherosclerotic lesions with areas of low or oscillating shear stress [4,40]. The workflow also permits visualization of the vessel's structural features as they are related to the hemodynamic results obtained from CFD. Figure 4 illustrates global velocity patterns at three points in time, which are used to calculate WSS, and shows important features. Figure 4(b) reveals the longest, darkest color vectors are observed immediately before peak systole. The low near-wall velocity observed in the inset images is consistent with assumed no-slip conditions at the wall. The regions of high TAWSS and low OSI near the bifurcation are consistent with the previous studies [41,42], and our method provides a means to visualize both antegrade and retrograde blood flow, as seen in Fig. 4(c) where the inset image shows flow separation by the downward (backward) pointing velocity vectors, which is thought to have clinical implications [43–45]. As expected, velocity magnitude decreases as the cycle progresses (Fig. 4(c)). Notice also the near-wall velocities are markedly less than the velocities near the vessel center at the entrance of the vessel and toward the inner wall downstream of the flow divider.

4.2 Case Study 2: LCX Coronary Artery. The second case study highlights results from the LCX as obtained with OCT. It has been shown that low WSS creates an environment favorable to the development of atherosclerotic or neointimal growth [46], and that these areas of low WSS can be characterized in vivo using the techniques described here. We can apply this method to in vivo patient data from two or more points in time to establish comparative data needed to quantitatively track disease

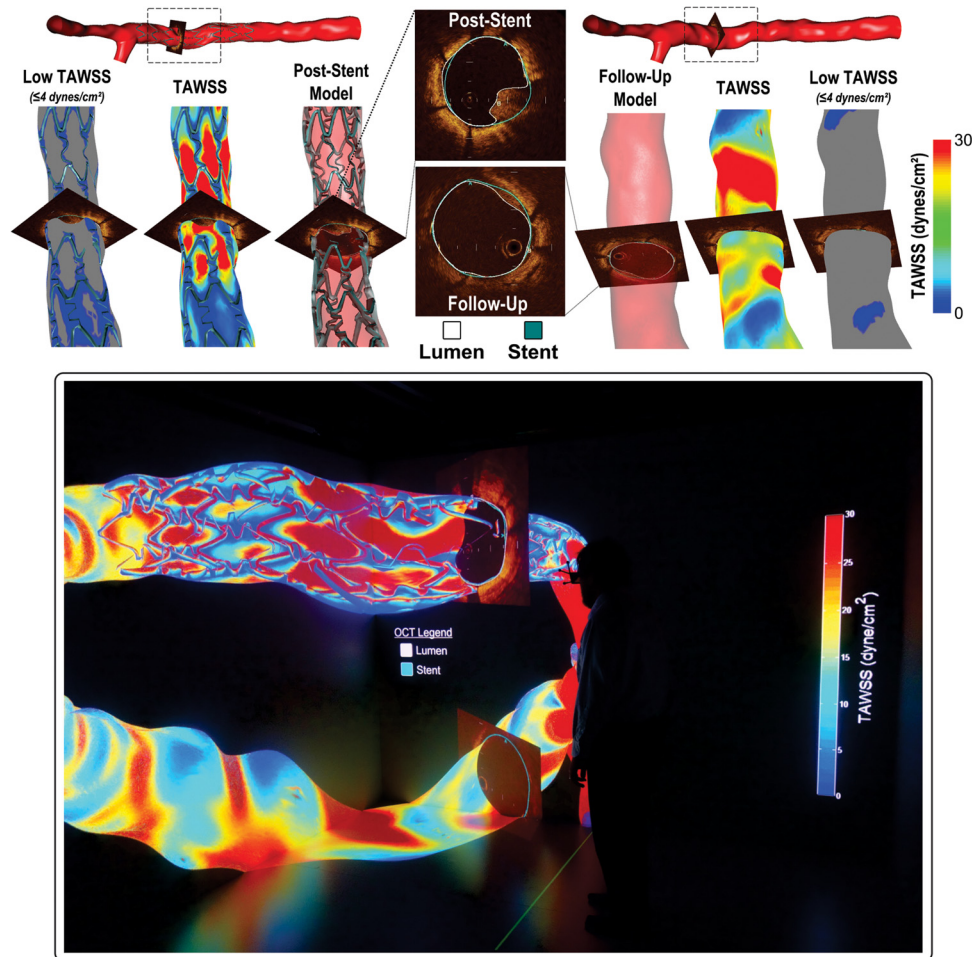


Fig. 6 IVE images showing CFD data at two time points- immediately following the stent implantation (left) and at 6-month follow-up (right). OCT was used to acquire all slices. A single OCT slice at corresponding locations is shown along with its relationship to TAWSS. A region of thrombus with high TAWSS after stenting (left) that subsequently remodels or migrates to yield a region of relatively diminished TAWSS (right) at 6-month follow-up is also shown. The images on the bottom of the figure show a user viewing OCT images and corresponding TAWSS results from the spatial location of interest where thrombus was observed after stenting. The poststenting immersive results are shown above the follow-up results.

progression. Figure 6 shows the same region of the vasculature with data captured at the time of stent placement (top left) and at 6-month follow-up (top right). Notice that the total surface area of low (≤ 4 dynes/cm²) TAWSS is decreased in the follow-up model. Importantly, features of an implanted stent including its geometric pattern and elution agent are thought to influence the results presented here and, thus, the likelihood for neointimal growth [47,48]. The use of IVEs for detailed analysis of these local vessel morphology and hemodynamics as presented here (Fig. 6 bottom) may be a key factor in further reducing rates of restenosis or thrombus formation [49] by representing a greater amount of spatial CFD results and how they change as a function of time. This practice can now be extended to include many models representing snapshots of vascular performance throughout the course of a longitudinal clinical study, or to track disease progression.

4.3 Limitations. The current methods should be considered relative to several potential limitations. First, the hardware and software used are specially designed for scientific visualization applications and may present issues of cost and availability. The current work was conducted in collaboration with Discovery World at Pier Wisconsin, a public facility with existing

visualization hardware and software. In most cases, a full-scale visualization center may be necessary to take full advantage of the workflow present here. However, similar advancements can be obtained incrementally as the level of sophistication and availability of visualization equipment increases from a basic 3D desktop monitor to a full-scale IVE. For example, we have ported CFD visualization results to a 3D desktop monitor using COVISE, a commercially available software package [34,50,51]. This allows multiple monitors to be linked together to form a tiled wall display. Such a display topology tends to be less expensive, and permits high-resolution analysis of results with stereoscopic rendering to provide improved depth cues, but without immersion.

Second, the IVE system featured here makes use of the CAVE layout generally consisting of between 4 and 6 screens in a cubic arrangement, each with one or more associated projectors and dedicated computers permitting stereoscopic viewing through active shutter glasses. However, the workflow and example applications presented here are not limited to this traditional CAVE style, but could also be implemented with larger tile-based display walls [52] or the more recent CAVE2 environment [53]. In contrast to the dimensions and arrangement for the traditional CAVE mentioned above, the CAVE2 is aligned in a circular arrangement (24 ft in diameter and 8 ft tall) that facilitates 320-deg panoramic

Table 3 General comparison of the differences afforded by viewing of CFD results with specialized software for use within a stereoscopic IVE as compared to a traditional non-IVE systems most often used with standard visualization software

		Approach	
	Simulation component	Traditional non-IVE	IVE
Input	Imaging data Vessel geometry	Volumetric and separately viewed CAD model with finite element mesh	Integrated slices with interactivity Finite element or discrete mesh
Output	Velocity Pressure Shear stress Temporal changes Viewing	Volume or stream tracings Mesh-mapped scalars Mesh-mapped vectors and scalars Slow with fewer time points Nonstereo, nonimmersive	Dynamic objects Textures Textures Rapid with more time points Stereoscopic and immersive

viewing. The CAVE2 system consists of 72 passive stereo off-axis-optimized 3D LCD panels with small bezels that are abutted (4 high and 18 around) to provide a resolution of 37 Megapixels in 3D.

Third, the workflow described here was only used with MR and OCT modalities and does not contain sufficient evidence that a visualization tool like IVE will have additional advantage over other established visualization tools for enhancing clinical decision-making. Formal rigorous testing needs to be performed in the future to establish absolute and relative clinical utility. We expect that as the method is refined and becomes robust through its use with other imaging modalities and application to additional pathologic conditions, potential barriers to viewing in IVEs will be mitigated and the application of this workflow to clinical outcomes will be explored further.

Fourth, the workflow is designed to accept CFD simulation results produced by the software tools used in our research group and may therefore need to be altered for use with other CFD packages. Fortunately there are many tools available to convert results into the VTK format because it is an open standard.

Finally, the use of EON STUDIO software to run the IVE presents the issues of cost and extensibility. The software carries acquisition and maintenance costs that might be mitigated through some open-source solutions such as the Blender Game Engine [54] or PARAVIEW [55]. However, the suggested benefits of viewing results for the clinical applications presented here are rooted in the two visualization elements of stereoscopic viewing and immersion. The ability to achieve both of these elements depends on the software and system being used (Table 3). For example, PARAVIEW is capable of running in stereo and can be clustered for use with CAVEs. However, when running PARAVIEW in stereo without a CAVE or other large scale system, immersion is lost and the user only has added depth cues. In contrast, when running PARAVIEW in the CAVE system, interactivity can be more limited than in the approach highlighted here, which facilitates setting a camera track for traveling within a vessel, instantaneous visualization of indices of interest at any location via key strokes, and the spatial localization and natural appearance of imaging data with the indices of interest. These operations may not be as straightforward to implement within traditional non-IVE scientific visualization packages and, consequently, seem to be very rarely performed. In contrast, additional ways of visualizing CFD results common to most traditional scientific visualization packages such as streamlines are not native to our IVE software, and future work will aim to incorporate this functionality.

5 Conclusion and Future Directions

We have developed a semi-automated workflow to integrate patient-specific CFD capabilities with an IVE capable of stereoscopic 3D rendering. In demonstrating the flexibility of the workflow, we have applied it to MR data of the LCCA where flow reversal and its relation to normal flow conditions as well as the colocalization of low TAWSS and atherosclerotic lesions were

visible. We also applied the workflow to the LCX, where we described the utility of our visualization method for exploring disease progression as quantified by the presence of low TAWSS regions and other markers described in the LCCA case. It is important to note that the workflow presented here makes use of the coordinate and connectivity data for the CFD simulations performed. Therefore, registration of post-treatment and follow-up CFD results can be conducted as may typically be performed by a user, and this spatiotemporal information will then be correctly positioned within the IVE when using the workflow.

It is worth mentioning that simply moving CFD results into the IVE forced the engineers, scientists, and clinicians involved in the current research to think carefully about the collection of data obtained, how more information can be extracted from associated CFD simulation results, and what the pipeline should be for rapidly identifying regions of interest for follow-up in longitudinal studies. While, in theory, some of this is also possible using desktop displays (with or without immersion), the prior literature surrounding cardiovascular CFD results suggests that it is not happening or only occurring in isolation. Future work will continue to mitigate potential barriers to viewing in IVEs using the current workflow, at which point clinical applications will be explored further in hopes of the workflow resulting in a clinically relevant tool.

Acknowledgment

The authors wish to thank Steve Atwell and Paul Krajniak of Discovery World at Pier Wisconsin for their support during development and presentation of the current results within the HIVE and Josh Hughey for technical assistance. The authors gratefully acknowledge Mark Bowers, Leanne Harmann, Robert Prost, Anil Vamsi Doppalapudi, Tayyab Mohyuddin, and Osama Zaidat for their contributions related to the LCCA data shown here. The authors similarly acknowledge Bon-Kwon Koo, Toshiro Shinke, Yasuhiro Honda, and Junya Shite for their contributions related to the LCX data shown here. Funding was provided by the Marquette University Department of Biomedical Engineering to David Quam.

References

- Hansson, G. K., 2005, "Inflammation, Atherosclerosis, and Coronary Artery Disease," *N. Engl. J. Med.*, **352**(16), pp. 1685–1695.
- Ku, D. N., Giddens, D. P., Zarins, C. K., and Glagov, S., 1985, "Pulsatile Flow and Atherosclerosis in the Human Carotid Bifurcation. Positive Correlation Between Plaque Location and Low Oscillating Shear Stress," *Arteriosclerosis*, **5**(3), pp. 293–302.
- Malek, A. M., Alper, S. L., and Izumo, S., 1999, "Hemodynamic Shear Stress and Its Role in Atherosclerosis," *JAMA*, **282**(21), pp. 2035–2042.
- Moore, J. E., Jr., Xu, C., Glagov, S., Zarins, C. K., and Ku, D. N., 1994, "Fluid Wall Shear Stress Measurements in a Model of the Human Abdominal Aorta: Oscillatory Behavior and Relationship to Atherosclerosis," *Arteriosclerosis*, **14**(2), pp. 225–240.
- Schroeder, W., Martin, K., Lorensen, B., Avila, L. S., Avila, R., and Law, C. C., 2006, *The Visualization Toolkit*, Kitware, Inc, Clifton Park, NY.

- [6] Chaudhry, A., Sutton, C., Wood, J., Stone, R., and McCloy, R., 1999, "Learning Rate for Laparoscopic Surgical Skills on Mist Vr, a Virtual Reality Simulator: Quality of Human-Computer Interface," *Ann. R. Coll. Surg. Engl.*, **81**(4), pp. 281–286.
- [7] Jordan, J. A., Gallagher, A. G., McGuigan, J., and McClure, N., 2001, "Virtual Reality Training Leads to Faster Adaptation to the Novel Psychomotor Restrictions Encountered by Laparoscopic Surgeons," *Surg. Endosc.*, **15**(10), pp. 1080–1084.
- [8] Steinman, D. A. H., and Steinman, D. A., 2007, "The Art and Science of Visualizing Simulated Blood-Flow Dynamics," *Leonardo*, **40**(1), pp. 71–76.
- [9] Drascic, D., Milgram, P., and Grodski, J., 1989, "Learning Effects in Telemanipulation with Monoscopic Versus Stereoscopic Remote Viewing," *IEEE International Conference on Systems, Man and Cybernetics*, Cambridge, MA, Nov. 14–17, pp. 1244–1249.
- [10] Ward, J. W., Phillips, R., Williams, T., Shang, C., Page, L., Prest, C., and Beavis, A. W., 2007, *Immersive Visualization With Automated Collision Detection for Radiotherapy Treatment Planning*, Studies in Health Technology and Informatics, IOS, Hull, UK.
- [11] Chu, J., Gong, X., Cai, Y., Kirk, M. C., Zusaq, T. W., Shott, S., Rivard, M. J., Melhus, C. S., Cardarelli, G., Hurley, A., Hepel, J. T., Napoli, J., Stutsman, S., and Abrams, R. A., 2009, "Application of Holographic Display in Radiotherapy Treatment Planning I: A Multi-Institutional Study," *J. Appl. Clin. Med. Phys.*, **10**(3), pp. 115–124.
- [12] Boejen, A., and Grau, C., 2011, "Virtual Reality in Radiation Therapy Training," *Surg. Oncol.*, **20**(3), pp. 185–188.
- [13] Votanopoulos, K., Bruniciardi, F. C., Thornby, J., and Bellows, C. F., 2008, "Impact of Three-Dimensional Vision in Laparoscopic Training," *World J. Surg.*, **32**(1), pp. 110–118.
- [14] Forsberg, A., Laidlaw, D. H., Van Dam, A., Kirby, R. M., Kafniadakis, G. E., and Elion, J. L., 2000, "Immersive Virtual Reality for Visualizing Flow Through an Artery," *Proceedings of Visualization*, Salt Lake City, UT, Oct. 13, pp. 457–460.
- [15] LaDisa, J. F., Jr., Bowers, M., Harmann, L., Prost, R., Doppalapudi, A. V., Mohyuddin, T., Zaidat, O., and Migrino, R. Q., 2010, "Time-Efficient Patient-Specific Quantification of Regional Carotid Artery Fluid Dynamics and Spatial Correlation With Plaque Burden," *Med. Phys.*, **37**(2), pp. 784–792.
- [16] Justice, J., Bergerud, M., Garrison, J., Cafiero, D., and Churches, L., 2009, *EON STUDIO 7*, EON Reality, Irvine, CA.
- [17] Murata, A., Wallace-Bradley, D., Tellez, A., Alviar, C., Aboodi, M., Sheehy, A., Coleman, L., Perkins, L., Nakazawa, G., Mintz, G., Kaluza, G. L., Virmani, R., and Granada, J. F., 2010, "Accuracy of Optical Coherence Tomography in the Evaluation of Neointimal Coverage after Stent Implantation," *JACC: Cardiovasc. Imaging*, **3**(1), pp. 76–84.
- [18] Ellwein, L. M., Otake, H., Gundert, T. J., Koo, B. K., Shinke, T., Honda, Y., Shite, J., and LaDisa, J. F., Jr., 2011, "Optical Coherence Tomography for Patient-Specific 3D Artery Reconstruction and Evaluation of Wall Shear Stress in a Left Circumflex Coronary Artery," *Cardiovasc. Eng. Technol.*, **2**(3), pp. 212–217.
- [19] Yarnykh, V. L., Terashima, M., Hayes, C. E., Shimakawa, A., Takaya, N., Nguyen, P. K., Brittain, J. H., McConnell, M. V., and Yuan, C., 2006, "Multicontrast Black-Blood MRI of Carotid Arteries: Comparison Between 1.5 and 3 Tesla Magnetic Field Strengths," *J. Magn. Reson. Imaging*, **23**(5), pp. 691–698.
- [20] Kerwin, W. S., Liu, F., Yarnykh, V., Underhill, H., Oikawa, M., Yu, W., Hatsukami, T. S., and Yuan, C., 2008, "Signal Features of the Atherosclerotic Plaque at 3.0 Tesla Versus 1.5 Tesla: Impact on Automatic Classification," *J. Magn. Reson. Imaging*, **28**(4), pp. 987–995.
- [21] Gundert, T. J., Shadden, S. C., Williams, A. R., Koo, B. K., Feinstein, J. A., and LaDisa, J. F., Jr., 2011, "A Rapid and Computationally Inexpensive Method to Virtually Implant Current and Next-Generation Stents Into Subject-Specific Computational Fluid Dynamics Models," *Annu. Biomed. Eng.*, **39**(5), pp. 1423–1437.
- [22] Muller, J., Sahni, O., Li, X., Jansen, K. E., Shephard, M. S., and Taylor, C. A., 2005, "Anisotropic Adaptive Finite Element Method for Modelling Blood Flow," *Comput. Methods Biomech. Biomed. Eng.*, **8**(5), pp. 295–305.
- [23] Sahni, O., Muller, J., Jansen, K. E., Shephard, M. S., and Taylor, C. A., 2006, "Efficient Anisotropic Adaptive Discretization of the Cardiovascular System," *Comput. Methods Appl. Mech. Eng.*, **195**(41–43), pp. 5634–5655.
- [24] Gundert, T. J., Dholakia, R. J., McMahon, D., and LaDisa, J. F., 2013, "Computational Fluid Dynamics Evaluation of Equivalency in Hemodynamic Alterations Between Driver, Integrity, and Similar Stents Implanted Into an Idealized Coronary Artery," *J. Med. Dev.*, **7**(1), p. 011004.
- [25] Williams, A. R., Koo, B. K., Gundert, T. J., Fitzgerald, P. J., and LaDisa, J. F., Jr., 2010, "Local Hemodynamic Changes Caused by Main Branch Stent Implantation and Subsequent Virtual Side Branch Balloon Angioplasty in a Representative Coronary Bifurcation," *J. Appl. Physiol.* (1985), **109**(2), pp. 532–540.
- [26] Wendell, D. C., Samyn, M. M., Cava, J. R., Ellwein, L. M., Krolkowski, M. M., Gandy, K. L., Pelech, A. N., Shadden, S. C., and LaDisa, J. F., Jr., 2013, "Including Aortic Valve Morphology in Computational Fluid Dynamics Simulations: Initial Findings and Application to Aortic Coarctation," *Med. Eng. Phys.*, **35**(6), pp. 723–735.
- [27] Holdsworth, D. W., Norley, C. J., Frayne, R., Steinman, D. A., and Rutt, B. K., 1999, "Characterization of Common Carotid Artery Blood-Flow Waveforms in Normal Human Subjects," *Physiol. Meas.*, **20**(3), pp. 219–240.
- [28] Gow, B. S., Schonfeld, D., and Patel, D. J., 1974, "The Dynamic Elastic Properties of the Canine Left Circumflex Coronary Artery," *J. Biomech.*, **7**(5), pp. 389–395.
- [29] Stergiopoulos, N., Meister, J. J., and Westerhof, N., 1994, "Simple and Accurate Way for Estimating Total and Segmental Arterial Compliance: The Pulse Pressure Method," *Annu. Biomed. Eng.*, **22**(4), pp. 392–397.
- [30] Stergiopoulos, N., Segers, P., and Westerhof, N., 1999, "Use of Pulse Pressure Method for Estimating Total Arterial Compliance In Vivo," *Am. J. Physiol.*, **276**(2 Pt 2), pp. H424–H428.
- [31] Vignon-Clementel, I. E., Figueroa, C. A., Jansen, K. E., and Taylor, C. A., 2006, "Outflow Boundary Conditions for Three-Dimensional Finite Element Modeling of Blood Flow and Pressure in Arteries," *Comput. Methods Appl. Mech. Eng.*, **195**(29–32), pp. 3776–3796.
- [32] Van Huis, G. A., Sipkema, P., and Westerhof, N., 1987, "Coronary Input Impedance During Cardiac Cycle as Determined by Impulse Response Method," *Am. J. Physiol.*, **253**(2 Pt 2), pp. H317–H324.
- [33] Esmaily-Moghadam, M., Bazilevs, Y., and Marsden, A. L., 2013, "A New Preconditioning Technique for Implicitly Coupled Multidomain Simulations With Applications to Hemodynamics," *Comput. Mech.*, **52**(5), pp. 1141–1152.
- [34] Quam, D. J., 2012, "Advanced Visualization and Intuitive User Interface Systems for Biomedical Applications," Master's thesis, Marquette University, Milwaukee, WI.
- [35] Cruz-Neira, C., Sandin, D. J., Defanti, T. A., Kenyon, R. V., and Hart, J. C., 1992, "The Cave: Audio Visual Experience Automatic Virtual Environment," *Commun. ACM*, **35**(6), pp. 64–72.
- [36] Slater, M., and Wilbur, S., 1997, "A Framework for Immersive Virtual Environments (Five): Speculations on the Role of Presence in Virtual Environments," *Presence Teleoperators Virtual Environ.*, **6**(6), pp. 603–616.
- [37] Van Dam, A., Forsberg, A., Laidlaw, D. H., Laviola, J. J., and Simpson, R. M., 2000, "Immersive VR for Scientific Visualization: A Progress Report," *IEEE Comput. Graphics Appl.*, **20**(6), pp. 26–52.
- [38] Presson, C. C., Delange, N., and Hazelrigg, M. D., 1987, "Orientation-Specificity in Kinesthetic Spatial Learning: The Role of Multiple Orientations," *Mem. Cogn.*, **15**(3), pp. 225–229.
- [39] Dede, C., 2009, "Immersive Interfaces for Engagement and Learning," *Science*, **323**(5910), pp. 66–69.
- [40] Gnasso, A., Irace, C., Carallo, C., De Franceschi, M. S., Motti, C., Mattioli, P. L., and Pujia, A., 1997, "In Vivo Association between Low Wall Shear Stress and Plaque in Subjects With Asymmetrical Carotid Atherosclerosis," *Stroke*, **28**(5), pp. 993–998.
- [41] Marshall, I., Zhao, S., Papathanasopoulou, P., Hoskins, P., and Xu, Y., 2004, "Mri and Cfd Studies of Pulsatile Flow in Healthy and Stenosed Carotid Bifurcation Models," *J. Biomech.*, **37**(5), pp. 679–687.
- [42] Zhao, S. Z., Xu, X. Y., Hughes, A. D., Thom, S. A., Stanton, A. V., Ariff, B., and Long, Q., 2000, "Blood Flow and Vessel Mechanics in a Physiologically Realistic Model of a Human Carotid Arterial Bifurcation," *J. Biomech.*, **33**(8), pp. 975–984.
- [43] Phillips, D. J., Greene, F. M., Jr., Langlois, Y., Roederer, G. O., and Strandness, D. E., Jr., 1983, "Flow Velocity Patterns in the Carotid Bifurcations of Young, Presumed Normal Subjects," *Ultrasound Med. Biol.*, **9**(1), pp. 39–49.
- [44] Nicholls, S. C., Phillips, D. J., Primozich, J. F., Lawrence, R. L., Kohler, T. R., Rudd, T. G., and Strandness, D. E., Jr., 1989, "Diagnostic Significance of Flow Separation in the Carotid Bulb," *Stroke*, **20**(2), pp. 175–182.
- [45] Steinke, W., Kloetzsch, C., and Hennerici, M., 1990, "Variability of Flow Patterns in the Normal Carotid Bifurcation," *Atherosclerosis*, **84**(2–3), pp. 121–127.
- [46] Stone, P. H., Coskun, A. U., Yeghiazarians, Y., Kinlay, S., Popma, J. J., Kuntz, R. E., and Feldman, C. L., 2003, "Prediction of Sites of Coronary Atherosclerosis Progression: In Vivo Profiling of Endothelial Shear Stress, Lumen, and Outer Vessel Wall Characteristics to Predict Vascular Behavior," *Curr. Opin. Cardiol.*, **18**(6), pp. 458–470.
- [47] Papafaklis, M. I., Bourantas, C. V., Theodorakis, P. E., Katsouras, C. S., Naka, K. K., Fotiadis, D. I., and Michalis, L. K., 2010, "The Effect of Shear Stress on Neointimal Response Following Sirolimus- and Paclitaxel-Eluting Stent Implantation Compared With Bare-Metal Stents in Humans," *JACC Cardiovasc. Interventions*, **3**(11), pp. 1181–1189.
- [48] LaDisa, J. F., Jr., Olson, L. E., Hettrick, D. A., Warltier, D. C., Kersten, J. R., and Pagel, P. S., 2005, "Axial Stent Strut Angle Influences Wall Shear Stress After Stent Implantation: Analysis Using 3D Computational Fluid Dynamics Models of Stent Foreshortening," *Biomed. Eng. Online*, **4**, p. 59.
- [49] Farooq, V., Gogas, B. D., and Serruys, P. W., 2011, "Restenosis: Delineating the Numerous Causes of Drug-Eluting Stent Restenosis," *Circ. Cardiovasc. Interventions*, **4**(2), pp. 195–205.
- [50] Quam, D. J., Ellwein, L. M., Otake, H., Migrino, R. Q., and LaDisa, J. F., 2011, "Mobile Virtual Reality System for Cardiovascular Cfd Analysis," *Biomedical Engineering Society (BMES) Annual Meeting*, Hartford, CT, Oct. 12–15, p. 56.
- [51] Aumüller, M., Lang, R., Rainer, D., Schulze, J. P., Werner, A., Wolf, P., and Wössner, U., 2008, *COVISE (Collaborative Visualization and Simulation Environment)*, Ver. 6.5, High Performance Computing Center Stuttgart, Universität Stuttgart, Stuttgart, DE.
- [52] Leigh, J., Renambot, L., Johnson, A., Jeong, B., Jagodic, R., Schwarz, N., Svistula, D., Singh, R., Aguilera, J., Wang, X., Vishwanath, V., Lopez, B., Sandin, D., Peterka, T., Girado, J., Kooima, R., Ge, J., Long, L., Verlo, A., Defanti, T. A., Brown, M., Cox, D., Patterson, R., Dorn, P., Wefel, P., Levy, S., Talandis, J., Reitzer, J., Prudhomme, T., Coffin, T., Davis, B., Wielinga, P., Stolk, B., Bum Koo, G., Kim, J., Han, S., Kim, J., Corrie, B., Zimmerman, T.,

- Boulanger, P., and Garcia, M., 2006, "The Global Lambda Visualization Facility: An International Ultra-High-Definition Wide-Area Visualization Collaboratory," *Future Gener. Comput. Syst.*, **22**(8), pp. 964–971.
- [53] Reda, K., Knoll, A., Nomura, K. I., Papka, M. E., Johnson, A. E., and Leigh, J., 2013, "Visualizing Large-Scale Atomistic Simulations in Ultra-Resolution Immersive Environments," Proceedings of the *IEEE* Symposium on Large-Scale Data Analysis and Visualization (LDAV'13), Atlanta, GA, Oct. 13–14, pp. 59–65.
- [54] Gascon, J., Bayona, J. M., Espadero, J. M., and Otaduy, M., 2011, "Blendercave: Easy Vr Authoring for Multi-Screen Displays," SIACG 2011: Ibero-American Symposium in Computer Graphics, Faro, Portugal, June 1–3.
- [55] Kitware, Inc., 2012, *PARAVIEW*.